INORGANIC CHEMISTRY
FRONTIERS

RESEARCH ARTICLE

View Article Online
View Journal | View Issue

Cite this: *Inorg. Chem. Front.*, 2025, **12**, 8445

Lanthanide contraction-driven modulation of photoswitchable macrocyclic complexes reveals unprecedented glass-induced re-isomerization and luminescence thermometry†

Dominika Prętka, *[a] Dawid Marcinkowski, [a] Nahir Vadra, [a] Przemysław Woźny, [a] Marcin Runowski, [a] Maciej Kubicki, [a] Violetta Patroniak, [a] Giuseppe Consiglio, [b] Giuseppe Forte [c] and Adam Gorczyński *[a]

Designing light-responsive supramolecular architectures with lanthanide ions offers a promising route towards multifunctional materials with tunable photophysical properties. Here, we report a systematic investigation across the lanthanide series of macrocyclic complexes incorporating azobenzene-functionalized diaza-crown ether ligands. We show that subtle changes in the ionic radius across the Ln^{3+} series dictate conformational preferences and modulate *trans*-to-*cis* photoisomerization efficiency under UV and visible light. Surprisingly, we uncover that the reverse *cis*-to-*trans* isomerization, which is here unresponsive to thermal or photonic stimuli, is uniquely triggered upon contact with glass surfaces, revealing a previously overlooked route for controlling molecular photoswitching. Additionally, selected complexes display efficient visible and near-infrared emission leveraged for robust luminescent thermometric behaviour in the solid state, with tunable sensitivity linked to the lanthanide ions. These findings advance the field of light-driven supramolecular materials and demonstrate how careful molecular-level design of lanthanide–azobenzene assemblies enables control over photoswitching, luminescence and thermal sensing properties, highlighting glass-mediated re-isomerization as a novel phenomenon with implications for future photoresponsive materials.

Received 8th July 2025,
Accepted 6th September 2025

DOI: 10.1039/d5qi01461a

rsc.li/frontiers-inorganic

1. Introduction

Light is a fundamental source of energy in photosynthesis, and harnessing light–matter interactions through artificial molecular systems opens pathways towards energy conversion and information processing at the molecular level. The design and synthesis of novel light-responsive supramolecular architectures are therefore of great importance for the development of smart, stimuli-responsive functional materials.[1,2] Advancing our understanding of these interactions through the engineering of new materials is a key scientific direction, with potential applications including electronic and optical devices,[3,4] data storage,[5–7] biological imaging, medical diagnostics, targeted drug delivery,[8,9] sensing,[10,11] encryption,[12] anti-counterfeiting technologies or multicolour QR codes.[1,13,14]

There is growing interest in the development of macrocyclic systems functionalized with photoswitchable units, as light offers a non-invasive and highly tunable stimulus for dynamic control over molecular conformation and properties in supramolecular assemblies.[15,16] Among the most widely used photoresponsive motifs is azobenzene, which undergoes reversible photoisomerization between two different geometric isomers – a linear *trans*-form and a bent *cis*-form – enabling the modulation of supramolecular photophysical behaviour.[13,17,18] Many light-responsive macrocycles incorporating azobenzene have been reported, though predominantly in metal-free systems.[19–25] When metal ions are introduced, coordination can either quench the photoswitching activity[26] or, conversely, enhance the selectivity and accelerate and improve control over the photoswitching processes.[27] This demonstrates a crucial role of matching energy levels and photochromic units to achieve effective and tunable photoswitchable behaviour.

Recent studies have highlighted the impact of transition metal ions in expanding the functionalities of light-responsive

[a]*Faculty of Chemistry, Adam Mickiewicz University in Poznań, Uniwersytetu Poznańskiego 8, 61-614 Poznań, Poland. E-mail: adam.gorczynski@amu.edu.pl*
[b]*Department of Chemical Science University of Catania, Via S. Sofia 64, 95125, Italy*
[c]*Department of Drug Science and Health University of Catania, Via S. Sofia 64, 95125, Italy*

†Dedicated to Professor Bronisław Marciniak on the occasion of his 75th birthday.

systems, enabling properties that are otherwise unattainable in purely organic frameworks.[28,29] In particular, integrating luminescent lanthanide ions with light-responsive molecules has emerged as a promising strategy to enhance both emission and photoswitching behaviour.[26,30–32] Switchable lanthanide complexes align well with the concept of multi-stimuli-responsive architectures, exhibiting sensitivity to light but also to chemical, thermal, electrical or mechanical inputs. This multifunctionality makes such materials increasingly desirable for applications in chemical sensing, cellular imaging, security tagging, and, most recently, as advanced luminescent optical thermometers.[12,33–36] In d-block systems, temperature shifts the balance between ligand- and metal-centered excited states and their nonradiative decay, with ratiometric intensity or lifetime being the thermometric readout (*e.g.* Re_2-L anions bridged with diamine-organic linkers[37] or $[Bz_2NH_2]_2[Mn(OC_6F_5)_4]$ ionic assembly[38]). In f-block complexes, the response often follows redistribution among crystal-field *mJ* sublevels and thermally assisted antenna-4f energy transfer, enabling self-calibrated intensity ratios, lifetimes or band-shape changes. Examples include a self-calibrated Dy^{3+} thermometer that also shows single-ion magnet (SIM) behaviour[39] or dinuclear single-molecule magnet (SMM) Nd^{3+} platforms linking ligation to thermometric performance.[40] Independent magneto-optical readouts can further improve thermal sensitivity.[41] Macrocyclic ligand designs further highlight multifunctionality: a Y^{3+}–diluted Dy^{3+} complex acts as a bifunctional SIM and luminescent thermometer, with both functions active below its blocking temperature,[42] and our Nd^{3+} macrocyclic SIM operates as a temperature-independent manometer and pressure-independent thermometer.[43] These precedents motivate the photoswitchable Nd^{3+}/Yb^{3+} macrocyclic complexes studied here and frame our analysis of how lanthanide contraction shapes their near-infrared thermometric response.

A number of azobenzene-functionalized lanthanide complexes have been reported to date, and their photoisomerization behaviour and structure–function relationships remain under active investigation.[44–53] However, comprehensive studies encompassing a broad range of lanthanide ions with organic ligands are still rare, limiting a deeper understanding of lanthanide contraction effects and their influence on structure and functionality in photoresponsive systems. Although lanthanide–macrocyclic complexes have been widely studied in fields such as biomedical imaging,[54,55] antenna-based emission systems,[55,56] and molecular nanomagnets (SMMs/SIMs),[55,57] the integration of photoswitchable units into such systems remains extremely limited. Lariat-type macrocycles bearing azobenzene moieties have primarily been developed for s-block metal ion coordination or membrane-mimetic applications,[24] while analogous systems with lanthanides are exceedingly rare.

In this work, we present a systematic study on a diaza-crown ether macrocycle functionalized with azobenzene units, **L-AzoH$_2$**, forming a distinct class of lanthanide complexes designed to investigate the structural and photophysical effects of lanthanide contraction. Despite the common quenching of azobenzene switching by metal coordination, our system retains efficient light-induced isomerization while exhibiting high stability of the *cis*-form—reverting to the *trans*-isomer unusually fast upon contact with the glass surface. Finally, representative complexes from both the *syn*- and *anti*-conformational families were evaluated as luminescent thermometers, establishing a novel correlation among macrocyclic geometry, switching behaviour and near-infrared emissive sensing across the lanthanide series (Fig. 1).

2. Results and discussion

2.1. Choice of the ligand, synthesis and characterization

The diaza-crown ether macrocyclic ligand was chosen because (1) macrocycles with N_2O_4 coordination cavities form stable

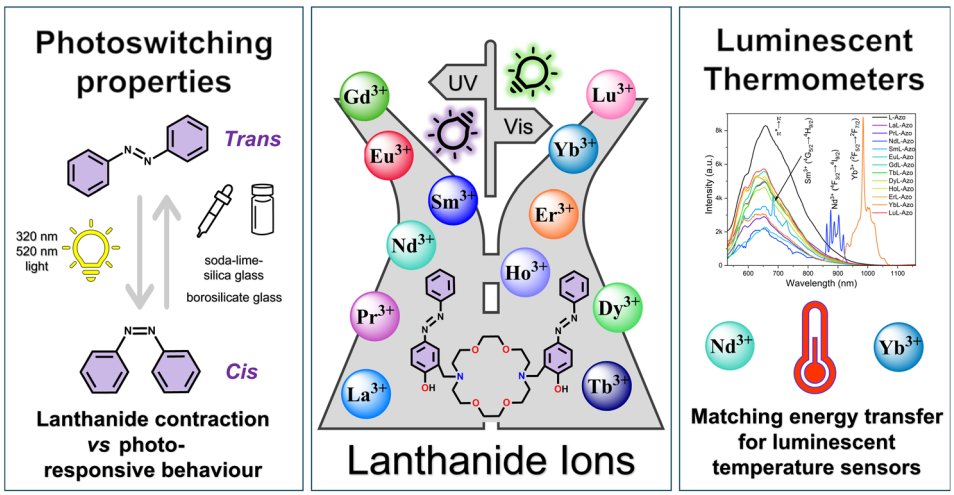

Fig. 1 An overview of key concepts covered in this work, which demonstrate the photoactive Ln-macrocyclic complexes in the context of lanthanide contraction.

lanthanide complexes and (2) allow symmetric functionalization with different groups, which should tune the photoresponsive properties. A pendant-arm azobenzene macrocyclic ligand named **L-AzoH$_2$** was obtained through the Mannich reaction, based on a previously reported procedure[58] with a slight modification of the purification method (section 1.3 in the SI). The purity and homogeneity were confirmed using Fourier transform infrared spectroscopy (FT-IR), electrospray mass spectrometry (ESI-MS), nuclear magnetic resonance spectroscopy (NMR) and thermogravimetric analysis (TGA) (Fig. S1–S7).

2.2. Design, synthesis and characterization of complexes

To understand the influence of interactions between the metal centers and the ligand molecule for the development of stimuli responsive azobenzene systems, we focused on the synthesis and investigation of compounds with lanthanide ions, which are interesting due to their emissive properties. To better understand the role of deprotonation of the ligand for photoresponsivity, a neutral Cu**L-Azo** system was also obtained. Simple complexes with a sodium ion, [Na**L-AzoH$_2$**]CF_3SO_3, and an uncoordinated ligand **L-AzoH$_2$** molecule were also used as references. The [Na**L-AzoH$_2$**]CF_3SO_3 complex was synthesized in an acetonitrile solution by the complexation reaction of the $NaCF_3SO_3$ salt with the **L-AzoH$_2$** ligand. Cu^{2+} and Ln^{3+} complexes were synthesized in a similar manner, in an acetonitrile (Cu**L-Azo**) or acetonitrile/methanol (Ln**L-Azo**CF_3SO_3) mixture (1 : 1, v : v) by the complexation reaction of the corresponding triflate salts with the **L-AzoH$_2$** ligand in the presence of triethylamine (Et_3N), used as a deprotonating agent (Fig. 2). A detailed description of the synthesis, isolation, and spectroscopic and solid-state characterization of the complexes can be found in the SI (sections 1.4 and 1.5). The FT-IR spectra (Fig. S8–S12) of the lanthanide complexes from La^{3+} to Lu^{3+} are almost identical, which confirmed high isostructurality in the solid state. This is also consistent with the mass spectra of these assemblies, as the peaks observed in the positive mode of the ESI-MS spectra indicate the formation of mononuclear complexes containing one **L-Azo** ligand molecule with two deprotonated OH groups from the azobenzene pendant-arms of the macrocycle for all complexes (Fig. S13–S24).

2.2.1. Single crystal and powder X-ray crystallography. Single crystals suitable for X-ray diffraction studies were obtained by slow evaporation of a dimethyl sulfoxide solution for the **L-AzoH$_2$** ligand, by the slow diffusion of diisopropyl ether into a solution of chloroform (Cu**L-Azo**) or acetonitrile/dichloromethane for lanthanide complexes Ln**L-Azo**CF_3SO_3 and by the slow diffusion of diisopropyl ether into a solution of acetonitrile for the [Na**L-AzoH$_2$**]CF_3SO_3 complex. For the sodium complex, two types of monocrystals were obtained under identical conditions, and they exhibited different space groups. Therefore, both structures were solved for comparison and designated as forms A and B, respectively.

Fig. 3 shows the comparison of the crystal structure of the free **L-AzoH$_2$** ligand molecule (a), its complex with a sodium ion with a non-deprotonated ligand (b) and a complex with Cu^{2+} with a deprotonated ligand form (c); the molecular structure of the lanthanide complex in the *syn*-conformation (d) and the packing diagram (e) of the La**L-Azo**CF_3SO_3 complex. The ligand molecule is C_i-symmetrical in the crystal structure, lying across the center of inversion in the space group $P2_1/c$ (Fig. 3a). The conformation of the macrocycle changes significantly upon complexation (Fig. 3b–d), and the change directs all N and O atoms towards the center of the complex. For the sodium complexes [Na**L-AzoH$_2$**]CF_3SO_3 (A and B), which are observed in both forms of different space group symmetries, $CF_3SO_3^-$ acts as a counterion and is not coordinated to the central metal ion. The coordination number of the sodium cation is in both cases 8 (N_2O_6), and the crystal lattices contain space which is filled by more (B) or less (A) ordered solvent molecules (Fig. 3b and Fig. S25). Fig. 3c shows the neutral Cu**L-Azo** complex, which is also centrosymmetric (C_i) with the Cu^{2+} ion located on an inversion centre. The metal ion is six-coordinated and is best described as a Jahn–Teller-elongated

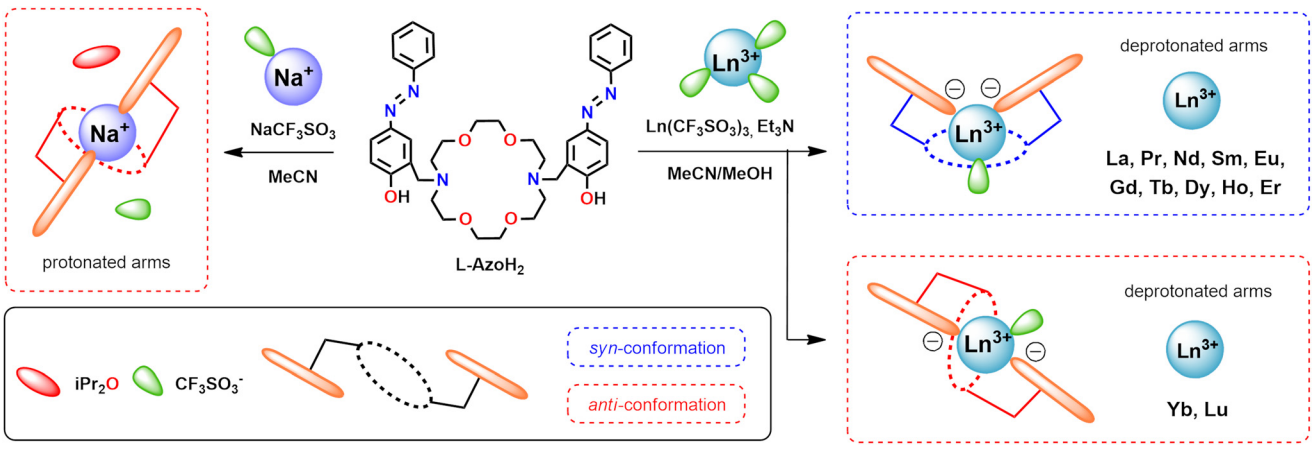

Fig. 2 Scheme for the synthesis of macrocyclic complexes with included conformations of the **L-AzoH$_2$** ligand scaffold.

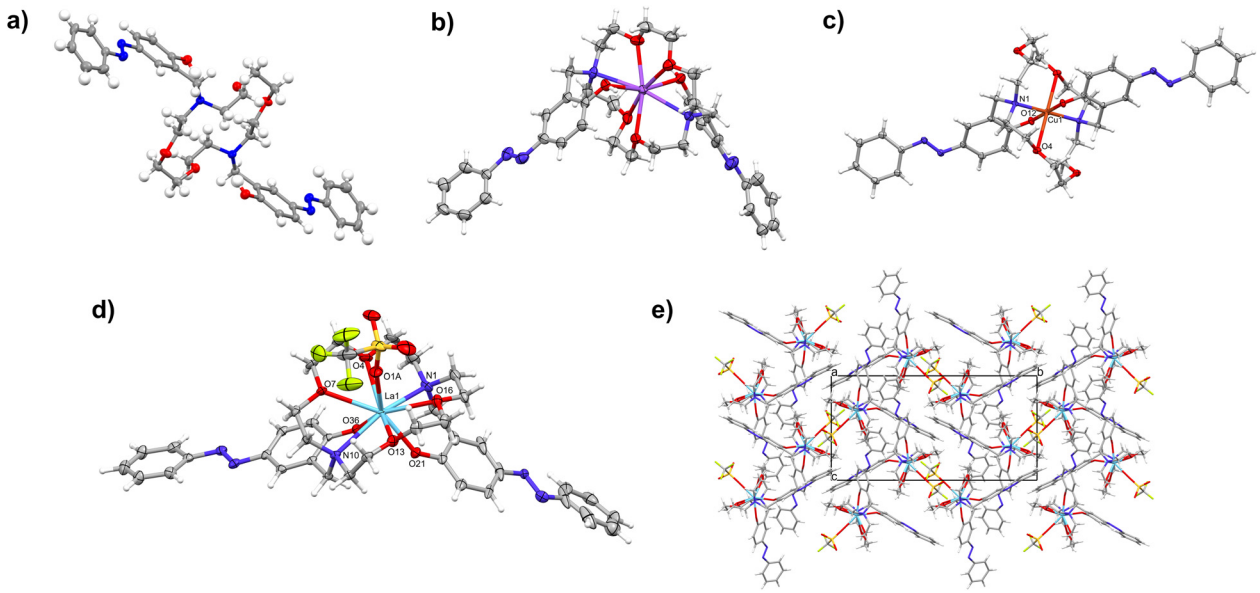

Fig. 3 Crystal structures of the (a) **L-AzoH$_2$** ligand; (b) [Na**L-AzoH$_2$**]CF_3SO_3 (A) complex; (c) Cu**L-Azo** complex; and (d) La**L-Azo**CF_3SO_3 complex; (e) packing diagram of the La**L-Azo**CF_3SO_3 complex.

octahedron (4 + 2): four donors define a nearly square equatorial plane, while two much longer axial Cu···O contacts complete the coordination sphere (see Table S4). Such pronounced axial elongation is typical of d^9 Cu^{2+} and is well precedented with over 4000 six-coordinated Cu^{2+} entries in the CSD displaying comparably unequal axial Cu–O distances.

The determined crystal structures for La**L-Azo**CF_3SO_3, Pr**L-Azo**CF_3SO_3, Nd**L-Azo**CF_3SO_3, Sm**L-Azo**CF_3SO_3, Eu**L-Azo**CF_3SO_3, Gd**L-Azo**CF_3SO_3, Tb**L-Azo**CF_3SO_3 and Er**L-Azo**CF_3SO_3 macrocyclic complexes have established that all Ln-assemblies are highly isostructural (Fig. 3d,e and Fig. S26–S32). They crystallize in the same space group ($P2_1/c$) and with very similar disposition of molecules in the crystal structure. The isostructurality goes so far that even a similar disorder of one of the dinitrogen bridges is found in all the structures. The lanthanide ion is 9-coordinated (quite typically) by two nitrogen and six oxygen atoms from the ligand molecule, four oxygen atoms from the macrocyclic ring and two oxygen atoms from the phenol moiety of the azobenzene pendant-arms, which are positioned at the same side of the macrocyclic unit resulting in a *syn* conformation. The coordination sphere is filled additionally by one oxygen atom from the coordinated triflate anion positioned at the opposite side of the two azobenzene pendant-arms of the macrocycle. We have recently demonstrated the crucial effect of a disordered triflate in the Nd^{3+}-macrocyclic assemblies for the implementation of multifunctional characteristics.[43] The crystal data, data collection, structure refinement and geometrical characteristics for the ligand and complexes are given in Tables S1–S4. The lanthanide contraction in the synthesized Ln-complexes influences the Ln–N and Ln–O bond distances, resulting in a general trend of gradual shortening of these bonds across the lanthanide series, with some exceptions to the expected trend (Table S4).

The powder X-ray diffraction (PXRD) patterns for La**L-Azo**CF_3SO_3, Pr**L-Azo**CF_3SO_3, Nd**L-Azo**CF_3SO_3, Sm**L-Azo**CF_3SO_3, Eu**L-Azo**CF_3SO_3, Gd**L-Azo**CF_3SO_3, Tb**L-Azo**CF_3SO_3 and Er**L-Azo**CF_3SO_3 complexes also confirmed their isostructurality. The experimental powder X-ray diffraction (PXRD) patterns of the lanthanide complexes were in accordance with simulated PXRD patterns based on single crystal diffraction data, indicating phase purity (Fig. S33). The differences in the sharpness and narrowness of the corresponding PXRD signals are due to the poor crystallinity of the powdered samples. In the case of the Dy**L-Azo**CF_3SO_3, Ho**L-Azo**CF_3SO_3, Yb**L-Azo**CF_3SO_3 and Lu**L-Azo**CF_3SO_3 complexes, the obtained samples are not in the crystalline state but in the amorphous phase, so their PXRD patterns were not possible to determine, but the experimental characterization confirmed their purity and uniformity (see section 1.5).

2.2.2. ^{1}H NMR spectroscopy. The La**L-Azo**CF_3SO_3 and Lu**L-Azo**CF_3SO_3 macrocyclic complexes were characterized using NMR spectroscopy (^{1}H, ^{13}C, and 2D NMR: COSY and HSQC) in $CDCl_3$ (Fig. S34–S41). The ^{1}H NMR spectra show significant differences from those of the free **L-AzoH$_2$** ligand in both aromatic and aliphatic regions, indicating coordination of the lanthanide ions through donor atoms of the macrocycle and azobenzene arms (Fig. 4). Both La^{3+} and Lu^{3+} complexes exist as single species in solution. The ^{1}H NMR spectrum of the La^{3+} complex is symmetric, indicating that the protons on both sides of the crown ether are chemically equivalent. This observation is consistent with X-ray crystallographic data, which show that the La^{3+} ion is centrally positioned within the macrocycle. In this complex, the azobenzene arms adopt a *syn*-conformation (both on the same side of the ring). In contrast, the Na^+ complex adopts an *anti*-conformation (arms on opposite sides), while also featuring a centrally located metal ion.

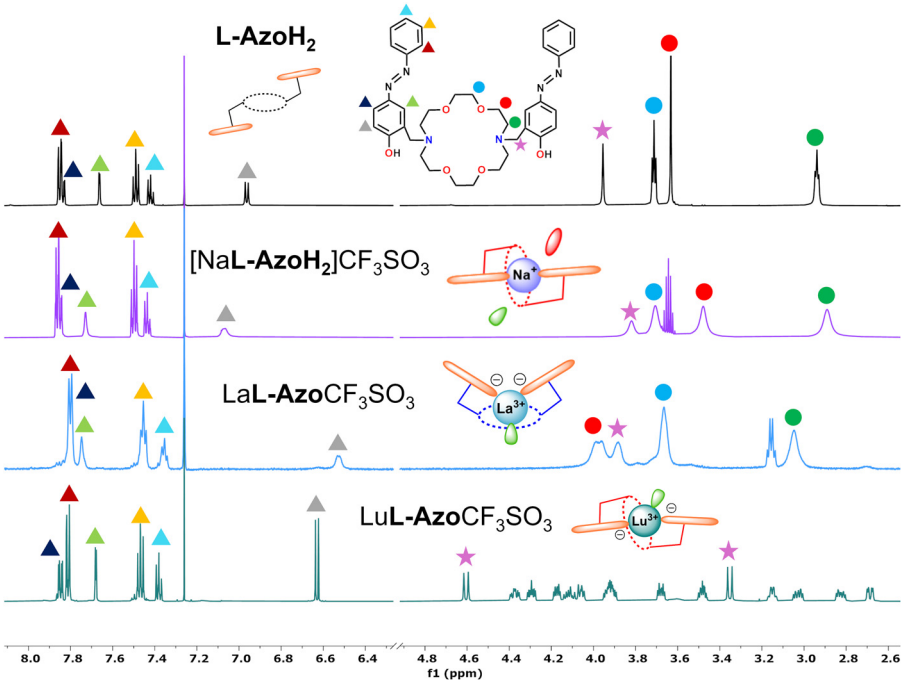

Fig. 4 Stacked ^{1}H NMR spectra for **L-Azo** (black), [Na**L-AzoH$_2$**]CF_3SO_3 (violet), La**L-Azo**CF_3SO_3 (blue) and Lu**L-Azo**CF_3SO_3 (green), along with a representation of the coordination around cations.

The broad signals in the aliphatic region of the ^{1}H NMR spectra for both the La^{3+} and Na^+ complexes are likely due to fast dynamic exchange processes. The Lu^{3+} complex shows an asymmetric ^{1}H NMR pattern, indicating a distinct structure. The smaller Lu^{3+} ion, due to lanthanide contraction, is likely coordinated asymmetrically and displaced from the macrocycle center (see section 2.4). The reorganization of the coordination environment around larger and smaller lanthanide ions and distinct conformational preferences in solution are recognized in the literature.[59–64]

Besides different conformations of the macrocycle cavity around the Ln centre in La^{3+} and Lu^{3+} assemblies, we suppose that the arrangement of coordinated azobenzene pendant-arms is also different. Firstly, the benzylic hydrogen resonances (methylene groups linking the crown moiety and azobenzene pendant-arms) differ between La^{3+} and Lu^{3+} complexes. These protons are a broad singlet in La^{3+}, while in Lu^{3+} they show a typical AX (δ_1 = 4.60 ppm; δ_2 = 3.35 ppm; J = 12.6 Hz; spectrometer frequency = 600 MHz; $\Delta\nu/J \sim 60$) spin system and resonate as doublets of doublets with significantly different chemical shifts. It indicates that benzylic protons are diastereotopic thanks to the different chemical environment. This result, together with the difference of the crown-ether signals, indicates that the latter complex is more rigid on the NMR timescale. Moreover, comparing the aromatic region, we can see that chemical shifts in the Lu^{3+} are more closely related to the ligand, where from the crystal structure data determination we observe that azobenzene pendant-arms are preorganized at the two opposite sides of the macrocyclic ligand skeleton (Fig. 3a). Integration of all these results allows us to predict that the azobenzene pendant arms adopt an *anti*-conformation in the Lu^{3+} complex. This is accompanied by a closely coordinated triflate anion near the Lu^{3+} center, which helps explain the observed conformational differences in solution. A comparison of energetic profiles *via* density functional theory (DFT) studies also supports the proposed *anti*-conformation in the Lu**L-Azo**CF_3SO_3 complex (see section 2.4).

2.3. Photoisomerization studies

2.3.1. *Trans*-to-*cis* isomerization. Due to the distinct shape and properties of the azobenzene molecule in its *trans*- and *cis*-forms, the characteristic absorption bands (π–π^* and n–π^*) for these two states of the molecules make them detectable.[1] The photoisomerization properties of the synthesized compounds were studied in chloroform solution and monitored using UV-vis absorption spectroscopy. Typically, *trans*-to-*cis* photoisomerization of the azobenzene moiety is induced by UV or visible light irradiation.[24,65] We demonstrate that incorporating a lanthanide metal center into the azobenzene macrocyclic ligand scaffold, **L-AzoH$_2$**, uncovers a light-responsive system with tunable photoswitchable properties. Investigation of the photoresponsive behaviour of the **L-AzoH$_2$** macrocycle in chloroform showed that the free ligand does not exhibit any photoswitching properties under UV (320 nm) or visible (520 nm) light, with no observable changes in the absorption spectrum (Fig. S42). Photoresponsive behaviour of the Nd**L-Azo**CF_3SO_3 macrocyclic complex in a chloroform solution has shown that this system is a dual-responsive supramolecular assembly, as the photoswitching and photochromic properties were observed under UV light (320 nm) and visible

light (520 nm). Upon irradiation of the Nd**L-Azo**CF_3SO_3 complex with 320 nm UV light, the absorbance of the π–π* band at 403 nm gradually decreases, with a noticeable appearance of the n–π* band as the intensity increases above 500 nm (Fig. 5a).

These dependencies are typical of the *trans*-to-*cis* isomerization of azobenzene molecules.[1,66] Therefore, this observation is an obvious confirmation of the UV light-induced isomerization to the *cis*-conformation of the azobenzene moiety in the Nd^{3+} macrocyclic complex. The photostationary state for the Nd^{3+} complex was reached after 3 h of irradiation, as indicated by intensity saturation of the band from the n–π* transition (Fig. 5a). We also revealed that the Nd^{3+} macrocyclic complex is sensitive to visible light irradiation, as exposure of the chloroform solution of the neodymium complex to 520 nm light irradiation induces the same photochromic and photoisomerization behaviour. This is indicated by identical changes in the absorption spectrum profile (Fig. 5b). The same rate of change from *trans* to *cis*-form under irradiation of the Nd^{3+} complex with visible light (4.00 mW cm^{-2}) compared to UV light (1.68 mW cm^{-2}) was observed after exposure to more intense light irradiation, as under the same conditions, the photoresponsive behaviour was practically invisible (for details, see section 1.1, in the SI). This suggests greater sensitivity to far UV light exposure, as *trans*-to-*cis* photoisomerization is faster even at a lower intensity of incident UV light (Fig. 5).

This led us to investigate whether **L-AzoH$_2$** photoisomerization properties depend on the nature of the metal ion and protonation state of the ligand. Accordingly, we studied the influence of s-block metal ion–Na^+ coordination and d-block metal ion–Cu^{2+} coordination in comparison with f-electron cation–Nd^{3+}. No evidence of the photoisomerization behaviour was observed for the [Na**L-AzoH$_2$**]CF_3SO_3 complex under exposure either to 320 nm or 520 nm light irradiation (Fig. S43a). *In situ* deprotonation of the ligand in the sodium complex also did not change these results (Fig. 43b). However, we observed that the copper complex (Cu**L-Azo**), with the ligand in its deprotonated form (for details, see sections 2.2.1, 1.4 and 1.5) exhibits reversible, photoswitchable behavior (Fig. S43c), though no visible colour change of the investigated solution was noted. Finally, *in situ* preparation of [$Nd(CF_3SO_3)_3$-**L-AzoH$_2$**] without deprotonation of the phenolic lariat arms also leads to a photoresponsive system, which is switched off after the demetallation of the system with excess trifluoroacetic acid (Fig. S43d). This demonstrates that photoisomerization of the azobenzene moiety is dependent on both the protonation state of the ligand (see also section 2.3.3) and the electronic nature of the metal ion.

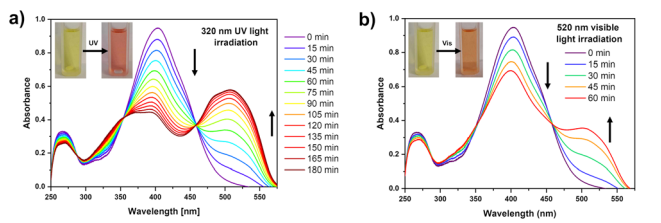

Fig. 5 UV-vis absorption spectra of the Nd**L-Azo**CF_3SO_3 complex as a function of irradiation time, measured after (a) 320 nm and (b) 520 nm light irradiation. The inset photographs show the colour change of the macrocyclic complex upon (a) UV and (b) visible light exposure of the Nd**L-Azo**CF_3SO_3 complex in chloroform solution.

2.3.2. Isomerization at different wavelengths and stability studies of the *cis*-form. While the Nd^{3+} macrocycle responds efficiently to 320 nm and 520 nm light, its photoisomerization under other wavelengths in the 340–720 nm range is negligible (Fig. S44a). A minor response appears in the 480–580 nm region, though significantly slower than the isomerization observed at 320 nm and 520 nm, where efficient isomerization to the *cis*-form occurs within 15 minutes (Fig. S44a). These findings confirm that 320 nm and 520 nm are the most effective excitation wavelengths, prompting us to select 320 nm for detailed characterization due to its comparable efficacy and experimental consistency.

Based on these results, we focused our investigation on the stability of the photoinduced *cis*-isomer and its reversibility to the thermodynamically favoured *trans*-isomer. We examined the influence of various external stimuli known to trigger *cis*-to-*trans* back-isomerization – *i.e.* light, heat and dark storage – on the stability of the *cis*-isomer and recovery of the *trans* form of the Nd^{3+} macrocyclic complex in solution. The *cis*-isomer remained highly stable at an elevated temperature (40 °C), showing no significant change in absorption intensity after 2 hours in a chloroform solution (Fig. 6a and Fig. S44b). Further temperature increase led to decomposition (Fig. S44b). Visible light irradiation across 380–720 nm failed to induce re-isomerization (Fig. S45a). Dark storage in a sealed quartz cuvette (wrapped in aluminium foil) also showed minimal recovery of the *trans* form after 24 hours, indicating high kinetic stability of the *cis* isomer (Fig. S45b). After 14 days of storage in the dark, the absorption band corresponding to the n–π* transition at ~505 nm decreased by about 50%, while the π–π* transition band at 403 nm recovered to 82% of its original *trans*-isomer intensity, indicating a very slow back-isomerization (Fig. 6b and Fig. S45b). These findings demonstrate the remarkable stability of the *cis*-form in the lanthanide macrocyclic complex, even under conditions typically efficient for the induction of back-isomerization of azobenzene based compounds. Surprisingly, we observed that repeatedly aspirating the *cis*-rich solution of the Nd^{3+} complex with a glass Pasteur pipette led to a visible colour change from orange to yellow, suggesting a return to the *trans*-form. Indeed, after 5 minutes of repeated pipetting, approximately 90% recovery of the *trans*-isomer was confirmed, regardless of whether the isomerization had originally been induced with 320 nm or 520 nm light (Fig. 6c and Fig. S46a, b).

2.3.3. Investigation of the underlying cause of the *cis*-to-*trans* re-isomerization mechanism. This unexpected observation prompted a series of control experiments to identify the underlying cause of the glass-induced re-isomerization. To test whether mechanical force was responsible, we subjected the

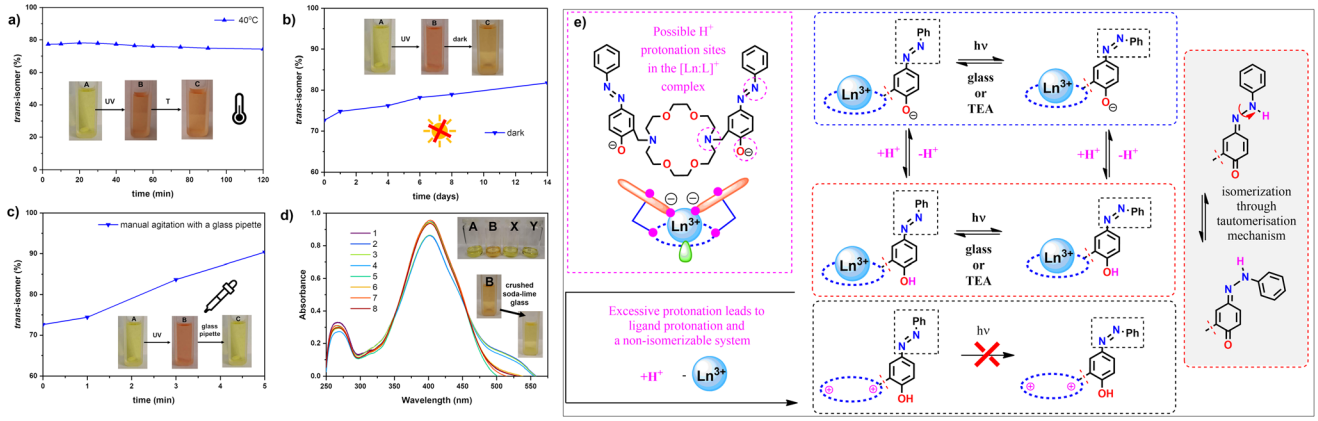

Fig. 6 Stability of the *cis*-isomer Nd^{3+} complex after 320 nm irradiation under varying conditions. (a) Effect of elevated temperature; (b) stability during dark storage; (c) manual agitation using a soda-lime-silicate glass pipette; (d) UV-vis absorption spectra illustrating the response to various stimuli: 1 – before irradiation, 2 – after 20 minutes of 320 nm UV irradiation, 3 – after 320 nm UV irradiation followed by 15 s shaking in a cuvette, 4 – manual agitation with a plastic pipette (5 min), 5 – manual agitation with a soda-lime-silicate glass pipette (5 min), 6 – shaking with a crushed soda-lime-silicate glass (15 s), 7 – manual stirring in a borosilicate or soda-lime-silicate vial (15 s), 8 – manual stirring in a silanized borosilicate vial (5 min). Colour changes (inserted photographs) – legend for figures a, b, c: A – before irradiation, B – after irradiation at 320 nm, C – temperature exposure (a), storage in the dark (b), contact with a glass pipette (c); for figure d: A – before irradiation, B – after irradiation at 320 nm, after 320 nm irradiation and stirring in borosilicate vial-X, or in soda-lime-silicate glass-Y. (e) Graphical representation of protonation and its effect on the photo-responsive behaviour of the macrocyclic lanthanide assemblies; for better demonstration of the process, the phenolic arm is presented as non-coordinating, but solution and solid state studies demonstrate coordination in the deprotonated form.

solution to ultrasonic treatment. However, this led to the decomposition of both *trans*- and *cis*-isomers of the complex (Fig. S47a). Stirring the solution with a magnetic stir bar or shaking the quartz cuvette had no effect on the absorption spectra or colour of the solution (Fig. 6d). The *cis*-isomer also remained stable in the presence of molecular oxygen (Fig. S47b) and manual pipetting with a plastic pipette (Fig. 6d). Furthermore, we demonstrated that transferring the orange *cis*-rich solution of the Nd^{3+} complex from a quartz cuvette into a borosilicate or soda-lime-silica vial and gently mixing for 15 seconds led to an immediate colour change to yellow, with full recovery of the *trans*-isomer absorption spectrum—consistent with results obtained *via* manual agitation using a glass pipette (Fig. 6d). Similarly, adding crushed soda-lime-silicate glass (sourced from a pipette) to the *cis*-rich solution and shaking for 15 seconds also triggered immediate colour change and restoration of the original absorption profile, indicating that the glass surface itself is responsible for the back-isomerization (Fig. 6d). To further investigate this, we added crushed soda-lime glass to the cuvette and left the sample undisturbed in the dark. A gradual return to the initial spectrum was observed after ~3 hours (Fig. S48a). These experiments collectively support the conclusion that the re-isomerization is not mechanically induced but rather driven by surface interactions with glass.

Intriguingly, although glass has been shown to accelerate certain chemical reactions,[67,68] this effect has not been reported for photochemical processes—particularly not for azobenzene-based photoswitches. To probe the origin of the glass-mediated re-isomerization, we examined the effect of individual components of the glass. A large excess of NaCl (500× molar) did not induce re-isomerization over 24 h, excluding Na^+ leached from the glass as an operative factor and suggesting that the lack of photoresponsivity of [Na**L-AzoH$_2$**]CF_3SO_3 arises from metal identity. Silanized borosilicate slowed the recovery of the *trans* isomer from *ca.* 15 s to *ca.* 5 min (Fig. 6d). Since silanization caps surface OH groups and suppresses formation of basic siloxide sites (SiO^-/M^+), this attenuation points to basic surface sites – not neutral Si–OH – as the active species. Consistently, adding even an excess of triphenyl silanol, Ph_3SiOH, to a *cis*-enriched solution produced no measurable effect (Fig. S48b). Finally, excess of borax triggered an immediate spectral recovery in a few seconds but led to a slow decomposition of the complex over 24 h (Fig. S48c), consistent with the basic character accelerating re-isomerization.

To assess whether protonation of phenoxide donors affects the photostationary state, we titrated a *cis*-rich Nd**L-Azo**CF_3SO_3 complex with acetic acid and trifluoroacetic acid (TFA). Acetic acid produced a modest increase in the *cis* fraction, and re-isomerization to *trans* remained inducible by glass contact (Fig. S48d). TFA increased the *cis* fraction at substoichiometric loadings, but once the acid exceeded *ca.* 0.5 equiv., it induced demetallation and the spectrum converged to that of the protonated ligand and the *trans* isomer with a loss of reversibility (Fig. S48e). In a *trans*-rich solution of Nd**L-Azo**CF_3SO_3, TFA likewise generated *cis*, which triethylamine (TEA) cleanly reverted; several cycles were feasible provided the acid remained below the demetallation threshold (Fig. S48f). Similar titration/irradiation cycles can be performed using glass instead of TEA (Fig. S48g). To probe direct protonation, we assembled a [$Nd(CF_3SO_3)_3$-**L-AzoH$_2$**] complex *in situ* and the

solution immediately adopted the *cis* state, remained switchable by glass back to *trans*, and was again re-enriched to *cis* upon 320 nm irradiation. Storage in the dark for 2 days increased the *cis* fraction, again recoverable to *trans* by glass or TEA (Fig. S48h and i). The spectra of *cis* generated by protonation and by 320 nm irradiation were indistinguishable within experimental uncertainty (Fig. S48j). To complement the UV-vis studies, we recorded ^{1}H NMR spectra on diamagnetic La^{3+} analogues (deprotonated La**L-Azo**CF_3SO_3 and the *in situ* assembled [$La(CF_3SO_3)_3$-**L-AzoH$_2$**]). These observations are qualitative only, due to concentration-related aggregation and higher concentrations required for NMR ($\geq 10^{-3}$ M *vs.* $\sim 10^{-5}$ M for UV-vis). Irradiation and acid/base/glass treatments produced diagnostic, reversible changes in the azobenzene-adjacent aromatic region consistent with *trans*/*cis* interconversions and protonation/deprotonation (Fig. S48k).

All data converge on the protonation–deprotonation mechanism that influences the photostationary state. Mild protonation (acetic acid; substoichiometric TFA) biases the system toward *cis*, consistent with the literature showing that protonation can facilitate azobenzene isomerization, in part by enabling the azo–hydrazone tautomerism and altering excited-state pathways.[69] In our system, we hypothesize that protonation of the phenolic lariat arms promotes intramolecular proton transfer to the azo group, generating a hydrazone-type tautomer in which the N–N single bond lowers the rotational barrier (Fig. 6e). This proposal is consistent with our observations that mild acid modestly enriches the *cis* form, strong acid initially increases *cis* but ≥0.5 equiv. induces demetallation, and that base/glass (SiO^-) restores the *trans*, deprotonated state. The *cis* state can likewise be generated photochemically (UV/Vis), whereas deprotonation restores the *trans* state. In this context, glass surfaces act as a benign heterogeneous base: interfacial SiO^- sites rapidly and reproducibly reintroduce the *trans* isomer without increasing the bulk pH or degrading the complex (Fig. 6d and Fig. S48d–k). Controls support this assignment: NaCl is inactive; silanized glass (fewer/basic sites) slows re-isomerization; a molecular silanol (Ph_3SiOH) has no effect; and borate/TEA also regenerates *trans* but can compromise stability with repeated cycles or higher loadings. Thus, glass functions as a solid–liquid "pH probe" and a gentle base, enabling *cis*/*trans* recovery that is otherwise difficult to achieve with chemical reagents.

These results demonstrate that Nd**L-Azo**CF_3SO_3 functions as a dual photoswitch, undergoing efficient *trans*-to-*cis* isomerization under both UV and visible light – an uncommon feature in azobenzene-based systems.[66,70–74] Strikingly, the reverse *cis*-to-*trans* isomerization cannot be triggered by conventional stimuli such as heat (40 °C), visible light (380–720 nm) or O_2[75] highlighting the high kinetic stability of the *cis*-form. Remarkably, we discovered that contact with glass surfaces induces rapid recovery of the *trans*-isomer, revealing an unprecedented case of glass surface catalyzed re-isomerization. This behaviour was consistent across all synthesized lanthanide series (see section 2.4), distinguishing our system from typical metal–azobenzene complexes and underscoring the critical role of ligand design and coordination environment in tuning the photoresponsive behaviour. Studies on related photoswitches are underway in our laboratory to ascertain if such an approach is compound specific or can be of general use and was up to now overlooked in the literature.

2.4. The effect of lanthanide contraction on structural formation and photoisomerization properties: DFT studies

The photoisomerization behaviour of the free **L-AzoH$_2$** ligand and the [Na**L-AzoH$_2$**]CF_3SO_3 and Cu**L-Azo** complexes, compared with that of the Nd**L-Azo**CF_3SO_3 system, highlights the critical role of the lanthanide ion in enabling light-responsive functionality. Coordination of Ln^{3+} ions to the macrocyclic scaffold significantly alters the electronic environment, directly impacting absorption profiles and photoisomerization efficiency.[76–79] Furthermore, structural variation across azobenzene-based metal complexes is known to affect their photochemical behaviour[28,80,81] so we examined photoisomerization across the lanthanide series accordingly.

The La**L-Azo**CF_3SO_3, Pr**L-Azo**CF_3SO_3, Sm**L-Azo**CF_3SO_3, Eu**L-Azo**CF_3SO_3, and Gd**L-Azo**CF_3SO_3 complexes exhibit photoisomerization behaviour similar to that of the Nd**L-Azo**CF_3SO_3 macrocyclic complex. All undergo efficient *trans*-to-*cis* switching under both 320 nm and 520 nm irradiation, accompanied by pronounced changes in absorption spectra and visible photochromic effects. *cis*-to-*trans* back-isomerization occurs rapidly *via* contact with glass surfaces, consistent across these early lanthanide complexes. Interestingly, they show greater sensitivity to UV light, with low-intensity 320 nm radiation yielding changes comparable to those induced by higher-intensity 520 nm light (Fig. S49–S53). A shift in behaviour appears with the Tb**L-Azo**CF_3SO_3 complex, which shows reduced switching under UV but improves responsiveness to 520 nm visible light (Fig. S54). For later lanthanides (Dy^{3+} to Lu^{3+}), 320 nm irradiation induces only minimal spectral changes, indicating suppressed photoisomerization under UV light (Fig. S55a–S59a). The efficiency of photoswitchable behaviour in Ln**L-Azo**CF_3SO_3 complexes is closely governed by the ionic radius of the lanthanide ion, reflecting the influence of lanthanide contraction. Based on this trend, the complexes can be broadly grouped into two categories. The first group (La^{3+} to Tb^{3+}) exhibits photoisomerization under both UV (320 nm) and visible (520 nm) light, with generally higher efficiencies under higher energy light, even at lower intensities (Fig. 7a – blue). Within this group, Tb^{3+} shows a noticeable decline in responsiveness. The second group (Dy^{3+} to Lu^{3+}) displays little to no response to UV irradiation, though some photoisomerization persists under visible light (Fig. 7a – green). Among the smallest ions (Ho^{3+}, Er^{3+}, Yb^{3+}, Lu^{3+}), the observed spectral changes and photochromism are minimal, underscoring a contraction-driven reduction in switching efficiency. Interestingly, it can be related to even smaller Cu^{2+} ions, further showing a combined influence of both the size and electronic nature of the chosen cation on the photoresponsiveness. It remains plausible that metal-dependent electronic structures (*e.g.*, heavy-atom/spin–orbit effects, ligand-

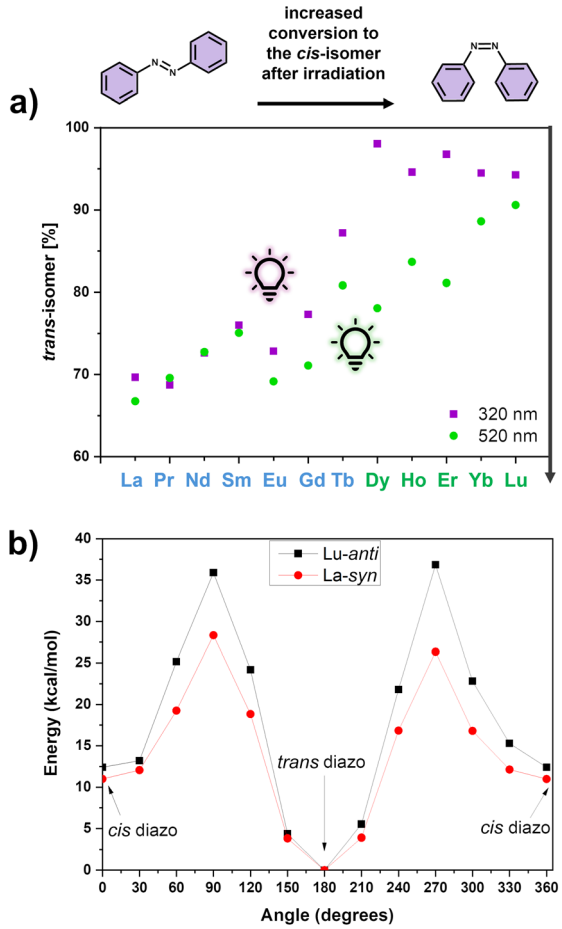

Fig. 7 (a) Schematic representation of how the lanthanide contraction phenomenon influenced the photoresponsive behaviour of specific groups of lanthanide-based macrocycles, (b) computed rotational energy profiles for azobenzene isomerization in *syn*-La**L-Azo**CF_3SO_3 (red circles) and *anti*-Lu**L-Azo**CF_3SO_3 (black squares) complexes, showing relative energy (kcal mol^{-1}) as a function of dihedral rotation angle (°) around the N=N bond. Both profiles display distinct minima at *cis* (0°, 360°) and *trans* (180°) geometries, with the *trans*-form being the global minimum in each case.

field coupling, and differences in nonradiative pathways) modulate the azobenzene excited-state landscape. Direct evidence would require time-resolved spectroscopy and electronic-structure calculations, which will be demonstrated in forthcoming studies.

These distinct behaviours prompted further investigation into the kinetics of photoisomerization across the series. The macrocyclic complexes Nd**L-Azo**CF_3SO_3 and Yb**L-Azo**CF_3SO_3 were chosen as representatives of the early and late lanthanides, respectively. Notably, the Yb^{3+} complex reached its photostationary state faster – after 105 minutes of irradiation – compared to 180 minutes for the Nd^{3+} analogue (Fig. S60 and Fig. 5a). The determined rate constants of the photoisomerization reaction for Nd**L-Azo**CF_3SO_3 (UV light – 320 nm) and Yb**L-Azo**CF_3SO_3 (visible light – 520 nm) were calculated as $k_{Nd} = 7.67 \times 10^{-5}$ s^{-1} and $k_{Yb} = 4.10 \times 10^{-5}$ s^{-1} respectively, using a first-order kinetic equation (Fig. S61). These values are lower than those typically reported for photoactive lanthanide complexes.[44–46,48,50,51] A comparison of the two reveals that the *syn*-configured Nd^{3+} complex switches more rapidly than the *anti*-configured Yb^{3+} analogue.

To explore the structural origin of this behaviour and the influence of lanthanide contraction, we optimized the geometry of the La**L-Azo**CF_3SO_3 complex based on its solid-state structure and modeled the lutetium analogue by substituting La^{3+} with Lu^{3+}—which was not available in crystalline form. In both models, the coordinating triflate anion was included, yielding nine-coordinate structures (Fig. S62). To validate the predicted structures, ^{1}HNMR chemical shifts were calculated for both conformers. The simulated spectra (Fig. S63) matched well with the experimental data. In the Lu^{3+} complex, methylene protons adjacent to the crown ether nitrogen atoms appeared at 3.2 and 4.6 ppm – consistent with the *anti*-conformation (compare with Fig. 4). The deshielding of the aromatic protons further supported this assignment, with a *para*-positioned proton shifting downfield to 7.83 ppm.

This structural differentiation aligns with the DFT-calculated isomerization energy profiles. Since *trans*/*cis* photoisomerization of the azobenzene moiety was experimentally observed to be wavelength dependent, the rotational barrier associated with the *trans*/*cis* isomerization was calculated. The same procedure was carried out for comparison with the La^{3+} complex in the *syn*-conformation, which isomerizes under both 320 nm and 520 nm irradiation and the results are shown in Fig. 7b. As observed and expected, the *trans*-isomer is more stable in both cases. Notably, the *anti*-configured Lu^{3+} complex is thermodynamically less stable than the *syn*-structure by 8.4 kcal mol^{-1}, suggesting that its formation is kinetically driven by the smaller ionic radius of Lu^{3+}. However, for the La^{3+} complex, the rotational barrier enabling *cis*-to-*trans* conversion is 16.49 kcal mol^{-1}, whereas for the Lu^{3+} complex, a higher barrier of 23.48 kcal mol^{-1} was calculated. The computed energy profiles reveal that the *anti*-Lu**L-Azo**CF_3SO_3 complex exhibits significantly higher isomerization barriers (~35 kcal mol^{-1}) than the *syn*-La**L-Azo**CF_3SO_3 analogue, consistent with the experimentally observed differences in photoisomerization efficiency. These findings collectively indicate that lanthanide contraction imposes rigidity and steric constraints around the azobenzene moiety, reducing conformational flexibility and suppressing photoisomerization.

2.5. Photoluminescence studies and luminescent temperature sensors

Based on the absorption characteristics, the luminescence properties of the sequence of lanthanide-based macrocyclic complexes were investigated in a solid-state form, using a 370 nm excitation source. It is noted that the investigated solid materials have a rigid structure; hence, they do not undergo isomerization and are stable under elevated temperature conditions, at least up to 220–270 °C (see the TGA – Fig. S64–S75), making them suitable candidates for optical sensing applications.

All of the lanthanide-based macrocyclic complexes show the characteristic broad emission band of the **L-AzoH$_2$** macrocyclic ligand (see the spectra for the **L-AzoH$_2$** ligand and complexes in Fig. S76 and S77), with a maximum at around 650 nm, as a result of the $\pi^* \rightarrow \pi$ transitions within the macrocyclic ligand (Fig. 8a). Photoluminescence intensity of the macrocyclic complexes decreases when Ln^{3+} ions are incorporated into the complex, which is evidence of ligand-to-metal energy transfer (LMET) from the **L-Azo** ligand to Ln^{3+} ions, as depicted in the energy level diagram in Fig. 8b. First, the deprotonated **L-Azo** ligand is excited by UV light from the singlet S_0 to S_1 state, then the intersystem crossing (ISC) process occurs, and the energy is transferred to the triplet state of the ligand. Finally, ligand emission from the excited T_1 state can be observed, together with a simultaneous LMET process, which results in the characteristic emission from Ln^{3+} ions.

Importantly, three of the Ln-based macrocyclic complexes show the characteristic Ln^{3+} ion emission bands, *i.e.* Sm**L-Azo**CF_3SO_3 ($\lambda \approx 680$ nm), Nd**L-Azo**CF_3SO_3 ($\lambda \approx 890$ nm) and Yb**L-Azo**CF_3SO_3 ($\lambda \approx 1000$ nm), as a result of the most efficient LMET process. These low-energy NIR-red emissions of the mentioned Ln^{3+} ions are observable because these Ln^{3+} ions have their emitting states located below (in energy) the lowest excited triplet state of the ligand. It is noteworthy that due to the same excitation mechanism for all complexes and inefficient direct excitation of the Ln^{3+} in complexes (forbidden 4f–4f transitions), the excitation spectra for all compounds are almost identical and exhibit the same excitation band, as shown in the exemplary spectrum shown in Fig. S76, which was used to estimate energies of S_1 and T_1 for the purpose of drawing the mentioned energy level diagram, indicating the possible radiative and nonradiative processes occurring in the studied system.

Following an initial evaluation, two materials with the most intense lanthanide emissions, *i.e.* Nd**L-Azo**CF_3SO_3 and Yb**L-Azo**CF_3SO_3 macrocyclic complexes, were selected, and their emission properties were investigated under varied temperature conditions, from cryogenic to high temperature, *i.e.*

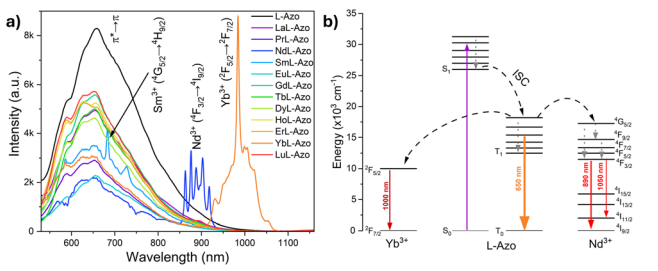

Fig. 8 (a) Emission spectra of the **L-AzoH$_2$** macrocyclic ligand (black), and Ln-based macrocyclic complexes in the solid-state form under 370 nm excitation. (b) Energy level diagram for the exemplary Nd**L-Azo**CF_3SO_3 and Yb**L-Azo**CF_3SO_3 macrocyclic complexes (continuous lines – emission; dotted arrows – multiphonon relaxation; dashed arrows – intersystem crossing and energy transfer).

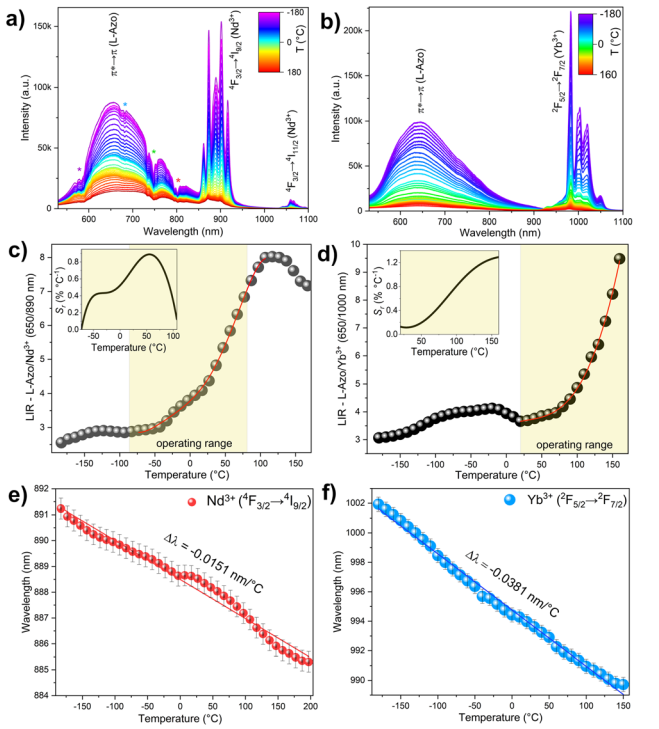

Fig. 9 (a and b) Emission spectra of the Nd**L-Azo**CF_3SO_3 (a) and Yb**L-Azo**CF_3SO_3 (b) complexes as a function of temperature; (c and d) the calculated LIRs for the Nd**L-Azo**CF_3SO_3 (c) and Yb**L-Azo**CF_3SO_3 (d) complexes; emission band centroids of Ln^{3+} for the Nd**L-Azo**CF_3SO_3 at ≈890 nm (e) and Yb**L-Azo**CF_3SO_3 at ≈1000 nm (f).

from −180 to 160 °C (Fig. 9). The first Nd**L-Azo**CF_3SO_3 macrocyclic complex shows a broad emission band in the visible (red) range, centred at ≈650 nm, associated with $\pi^* \rightarrow \pi$ transition from the macrocyclic part of the complex, as well as sharp emission bands from Nd^{3+} at around 890 nm ($^4F_{3/2} \rightarrow {}^4I_{9/2}$) and 1050 nm ($^4F_{3/2} \rightarrow {}^4I_{11/2}$), accompanied by characteristic narrow peaks due to crystal-field split *mJ* sublevels (Fig. 9a). It is noteworthy that, in this case, the influence of the Nd^{3+} absorption is also clearly visible in the form of intensity drops (due to Nd^{3+} reabsorption) at around 580, 670, 750 and 800 nm ($^4I_{9/2} \rightarrow {}^2G_{9/2}$, $^4F_{9/2}$, $^2G_{7/2}$ and $^4F_{5/2}$ Nd^{3+} transitions, respectively), altering the expected round shape of the broad emission band ($\pi^* \rightarrow \pi$) from the organic component.

The gradual decrease of luminescence intensity of the deprotonated **L-Azo** ligand and Nd^{3+} as a function of temperature is a result of thermal quenching of emission in a nonradiative way (inset in Fig. 9a).[82,83] A similar tendency was observed for the Yb**L-Azo**CF_3SO_3 macrocyclic complex in Fig. 9b. However, the change of intensity for both bands (**L-Azo** and Ln^{3+}) was not the same; hence, we could calculate the luminescence intensity ratio (LIR) parameter for both macrocyclic complexes, which can work as a thermometric parameter utilized in optical thermometry. The LIR between two emission bands of the **L-Azo** ligand and Ln^{3+} ions (*i.e.* **L-Azo**/Nd^{3+} and **L-Azo**/Yb^{3+}) changes monotonously from around −70 to 110 °C for the Nd^{3+} complex and from 20 to

160 °C for the Yb^{3+} complex, allowing their use as luminescent thermometers in the indicated operating temperature ranges (Fig. 9c and d). Based on the calculated thermometric parameters, we also calculated the relative thermal sensitivity (S_r) of the developed sensors using eqn (1):

$$S_r = \frac{\partial \mathrm{LIR}}{\partial T} \times \frac{1}{\mathrm{LIR}} \times 100\% \quad (1)$$

The S_r parameter for the Nd**L-Azo**CF_3SO_3 complex reaches the maximum value of ≈0.89%/°C at around 55 °C (see the inset in Fig. 9c). However, for the Yb**L-Azo**CF_3SO_3 complex, the S_r parameter has the maximum value of ≈1.289% per °C at the highest operating temperature, *i.e.* at 160 °C (see the inset in Fig. 9d).

Another observed temperature-dependent spectroscopic effect is the spectral shift with temperature. In both materials the spectral position of the **L-Azo** moiety emission band changes non-monotonously with temperature (data not shown), in contrast to the emission band centroids for the Nd^{3+} and Yb^{3+}, which linearly change with temperature. Both emission bands, centered at $\lambda \approx 890$ nm for Nd^{3+} and at $\lambda \approx 1000$ nm for Yb^{3+}, show a linear blue-shift, with a rate $\Delta\lambda = -0.0151$ and -0.0381 nm $°C^{-1}$, respectively, caused by the thermal expansion of the unit cell. Specifically, the observed spectral shift is due to the static contribution caused by the changes in the site geometry, which is occupied by the lanthanide ion in the crystal, as a result of lattice thermal expansion.[82,84] The observed spectral shifts, together with the discussed LIRs allow multi-parameter temperature sensing in a relatively broad *T*-range. It is worth noting that due to severe quenching of Ln^{3+} luminescence by the solvent molecules, the characteristic emission bands originating from Ln^{3+} ions could be observed only in the solid-state form of the metal–organic complexes studied (see Fig. S78 for comparison). Nonetheless, broad ligand centered emission overlaps the region typically used to excite the *cis* n → π* band and could possibly be the reason visible irradiation does not drive efficient *cis*/*trans* re-isomerization. While metal coordination, aggregation effects and matrix rigidity may also play a role in this, a definitive mechanism will require time-resolved and solvent-dependent studies that are beyond the scope of this study.

3. Conclusions

We report the development of a new class of photoswitchable lanthanide-based macrocyclic complexes, where *trans*-to-*cis* isomerization is induced by light and reversed through an unprecedented glass surface-mediated mechanism. Structural and spectroscopic studies across the Ln**L-Azo**CF_3SO_3 series revealed two distinct structural regimes. Complexes from La^{3+} to Tb^{3+} and Er^{3+} adopt a consistent nine-coordinate geometry comprising donor atoms from the diazacrown ether, azobenzene moiety and a monodentate triflate anion. Despite this apparent structural consistency, ^{1}H NMR and DFT studies identified a conformational shift from a *syn*- to *anti*-arrangement as the lanthanide series progresses – correlated with increased ligand rigidity and higher isomerization barriers.

All synthesized Ln-complexes display light-responsive behaviour, with most undergoing reversible *trans*-to-*cis* photoisomerization in solution under UV and/or visible light irradiation. Switching efficiency depends on the nature of the lanthanide ion and its electronic structure, with suppression observed in certain cases, particularly for smaller lanthanides, aligning with computational findings and highlighting the impact of lanthanide contraction on the photoswitching dynamics. Notably, the reverse *cis*/*trans* isomerization proved unresponsive to conventional triggers such as heat, visible light, or oxygen, but it occurred rapidly upon contact with the glass surface. This unusual recovery combined with the high stability of the *cis*-isomer introduces an unprecedented case of glass-driven re-isomerization of diazobenzene photoswitches and can be explained on the basis of protonation/deprotonation behaviour.

In addition to the photoresponsive solution behaviour, the solid-state luminescence properties of the complexes were also investigated, with Nd^{3+} and Yb^{3+} complexes exhibiting promising thermosensitive emissions. These systems function as dual VIS/NIR luminescent thermometers, based on LIR and band shifts, representing the first example of such dual photoswitchable and luminescent macrocyclic systems. The combined study of isomerization and emission behaviour under light irradiation underscores the potential of these macrocycles as multi-stimuli-responsive lanthanide platforms. This work provides new insights into the interplay between macrocyclic conformation, metal ion size and external stimuli, offering a valuable design strategy for future development of functional lanthanide-based supramolecular materials.

Author contributions

Dominika Prętka: conceptualization, data curation, investigation, visualization, writing – original draft, and writing – review & editing; Dawid Marcinkowski: formal analysis and resources; Nahir Vadra: investigation and resources; Przemysław Woźny: data curation, investigation, and writing – original draft; Marcin Runowski: conceptualization, visualization, writing – review & editing, and resources; Maciej Kubicki: data curation, formal analysis, visualization, and writing – original draft; Violetta Patroniak: supervision, resources, visualization, and writing – review & editing; Giuseppe Consiglio: formal analysis, methodology, and writing – review & editing; Giuseppe Forte: formal analysis, methodology, and writing – review & editing; Adam Gorczyński: conceptualization, methodology, investigation, visualization, writing – original draft, writing – review & editing, project administration, supervision, resources, and funding acquisition.

Conflicts of interest

There are no conflicts to declare.

Data availability

The data supporting this article have been included as part of the SI and are also available in the public open repository Zenodo at **https://doi.org/10.5281/zenodo.15790031**.

Supplementary information is available. See DOI: **https://doi.org/10.1039/d5qi01461a**.

CCDC 2406250–2406258, 2435298, 2435299 and 2480151 contain the supplementary crystallographic data for this paper.[85a–l]

Acknowledgements

We acknowledge B.Sc. Antoni Stefaniak for help in the synthesis of the Cu**L-Azo** complex. This work was supported by the National Science Centre, Poland (grant no. 2020/39/D/ST4/01182 (PI: A. G.), 2022/45/N/ST4/00344 (PI: D. M.), 2023/50/E/ST5/00021 (PI: M. R.), 2024/52/C/ST5/00047 (PI: N. V.)).

References

1 M. Baroncini, J. Groppi, S. Corra, S. Silvi and A. Credi, Light-Responsive (Supra)Molecular Architectures: Recent Advances, *Adv. Opt. Mater.*, 2019, **7**, 1900392.
2 Z. Yang, Z. Liu and L. Yuan, Recent Advances of Photoresponsive Supramolecular Switches, *Asian J. Org. Chem.*, 2021, **10**, 74–90.
3 T. Zheng, M. Runowski, I. R. Martín, K. Soler-Carracedo, L. Peng, M. Skwierczyńska, M. Sójka, J. Barzowska, S. Mahlik, H. Hemmerich, F. Rivera-López, P. Kulpiński, V. Lavín, D. Alonso and D. Peng, Mechanoluminescence and Photoluminescence Heterojunction for Superior Multimode Sensing Platform of Friction, Force, Pressure, and Temperature in Fibers and 3D-Printed Polymers, *Adv. Mater.*, 2023, **35**, 2304140.
4 C. Hernández-Álvarez, P. I. Martín-Hernández, I. R. Martín, F. Rivera-López, H. Hemmerich, M. Grzegorczyk, S. Mahlik and M. Runowski, Optical Temperature Sensor Evaluation in a Working Gear Motor: Application of Luminescence Thermometry in Industrial Technology, *Adv. Opt. Mater.*, 2024, **12**, 2303328.
5 X. Yao, T. Li, J. Wang, X. Ma and H. Tian, Recent Progress in Photoswitchable Supramolecular Self-Assembling Systems, *Adv. Opt. Mater.*, 2016, **4**, 1322–1349.
6 A. Goulet-Hanssens, F. Eisenreich and S. Hecht, Enlightening Materials with Photoswitches, *Adv. Mater.*, 2020, **32**, 1905966.
7 X. Huang and T. Li, Recent progress in the development of molecular-scale electronics based on photoswitchable molecules, *J. Mater. Chem. C*, 2020, **8**, 821–848.
8 I. M. Welleman, M. W. H. Hoorens, B. L. Feringa, H. H. Boersma and W. Szymański, Photoresponsive molecular tools for emerging applications of light in medicine, *Chem. Sci.*, 2020, **11**, 11672–11691.
9 S. Jia, W.-K. Fong, B. Graham and B. J. Boyd, Photoswitchable Molecules in Long-Wavelength Light-Responsive Drug Delivery: From Molecular Design to Applications, *Chem. Mater.*, 2018, **30**, 2873–2887.
10 T. Zheng, J. Luo, D. Peng, L. Peng, P. Woźny, J. Barzowska, M. Kamiński, S. Mahlik, J. Moszczyński, K. Soler-Carracedo, F. Rivera-López, H. Hemmerich and M. Runowski, Persistent Photoluminescence and Mechanoluminescence of a Highly Sensitive Pressure and Temperature Gauge in Combination with a 3D-Printable Optical Coding Platform, *Adv. Sci.*, 2024, **11**, 2408686.
11 L. Marciniak, P. Woźny, M. Szymczak and M. Runowski, Optical pressure sensors for luminescence manometry: Classification, development status, and challenges, *Coord. Chem. Rev.*, 2024, **507**, 215770.
12 M. Runowski, P. Woźny, I. R. Martín, K. Soler-Carracedo, T. Zheng, H. Hemmerich, F. Rivera-López, J. Moszczyński, P. Kulpiński and S. Feldmann, Multimodal Optically Nonlinear Nanoparticles Exhibiting Simultaneous Higher Harmonics Generation and Upconversion Luminescence for Anticounterfeiting and 8-bit Optical Coding, *Adv. Funct. Mater.*, 2024, **34**, 2307791.
13 M. Younis, S. Ahmad, A. Atiq, M. Amjad Farooq, M.-H. Huang and M. Abbas, Recent Progress in Azobenzene-Based Supramolecular Materials and Applications, *Chem. Rec.*, 2023, **23**, e202300126.
14 Z.-H. Liao and F. Wang, Light-controlled smart materials: Supramolecular regulation and applications, *Smart Mol.*, 2024, e20240036.
15 E. Nieland, J. Voss and B. M. Schmidt, Photoresponsive Supramolecular Cages and Macrocycles, *ChemPlusChem*, 2023, **88**, e202300353.
16 C. Ludwig and J. Xie, The Growing Field of Photoswitchable Macrocycles: A Promising Way to Tune Various Properties with Light, *ChemPhotoChem*, 2023, **7**, e202300126.
17 C. Fedele, T.-P. Ruoko, K. Kuntze, M. Virkki and A. Priimagi, New tricks and emerging applications from contemporary azobenzene research, *Photochem. Photobiol. Sci.*, 2022, **21**, 1719–1734.
18 F. A. Jerca, V. V. Jerca and R. Hoogenboom, Advances and opportunities in the exciting world of azobenzenes, *Nat. Rev. Chem.*, 2022, **6**, 51–69.
19 S. Song, H. Zhang and Y. Liu, Light-Controlled Macrocyclic Supramolecular Assemblies and Luminescent Behaviors, *Acc. Mater. Res.*, 2024, **5**, 1109–1120.
20 J. Yu, D. Qi and J. Li, Design, synthesis and applications of responsive macrocycles, *Commun. Chem.*, 2020, **3**, 189.
21 Z. Li, J. Liang, W. Xue, G. Liu, S. H. Liu and J. Yin, Switchable azo-macrocycles: from molecules to functionalisation, *Supramol. Chem.*, 2014, **26**, 54–65.
22 W.-C. Geng, H. Sun and D.-S. Guo, Macrocycles containing azo groups: recognition, assembly and application, *J. Inclusion Phenom. Macrocyclic Chem.*, 2018, **92**, 1–79.
23 H. Roithmeyer, M. Uudsemaa, A. Trummal, M.-L. Brük, S. Krämer, I. Reile, V. Rjabovs, K. Palmi, M. Rammo,

R. Aav, E. Kalenius and J. Adamson, Large Azobenzene Macrocycles: Formation and Detection by NMR and MS Methods, *Supramol. Chem.*, 2023, **34**, 77–86.

24 E. Wagner-Wysiecka, N. Łukasik, J. F. Biernat and E. Luboch, Azo group(s) in selected macrocyclic compounds, *J. Inclusion Phenom. Macrocyclic Chem.*, 2018, **90**, 189–257.

25 P. Tecilla and D. Bonifazi, Configurational Selection in Azobenzene-Based Supramolecular Systems Through Dual-Stimuli Processes, *ChemistryOpen*, 2020, **9**, 529–544.

26 O. Galangau, L. Norel and S. Rigaut, Metal complexes bearing photochromic ligands: photocontrol of functions and processes, *Dalton Trans.*, 2021, **50**, 17879–17891.

27 R. G. DiNardi, A. O. Douglas, R. Tian, J. R. Price, M. Tajik, W. A. Donald and J. E. Beves, Visible-Light-Responsive Self-Assembled Complexes: Improved Photoswitching Properties by Metal Ion Coordination, *Angew. Chem., Int. Ed.*, 2022, **61**, e202205701.

28 G. C. Thaggard, J. Haimerl, K. C. Park, J. Lim, R. A. Fischer, B. K. P. Maldeni Kankanamalage, B. J. Yarbrough, G. R. Wilson and N. B. Shustova, Metal–Photoswitch Friendship: From Photochromic Complexes to Functional Materials, *J. Am. Chem. Soc.*, 2022, **144**, 23249–23263.

29 M. A. Soto and M. J. MacLachlan, Responsive macrocyclic and supramolecular structures powered by platinum, *Chem. Sci.*, 2024, **15**, 431–441.

30 L. Su, X. Liu, Q. Niu and Z. Li, Photoresponsive lanthanide luminescent materials, *J. Mater. Chem. C*, 2024, **12**, 10759–10774.

31 Y. Fréroux, L. Caussin, N. El Beyrouti, S. Rigaut and L. Norel, in *Handb. Phys. Chem. Rare Earths*, ed. J.-C. G. Bünzli and S. M. Kauzlarich, Elsevier, 2024, vol. 65, pp. 35–91.

32 Y. Hasegawa, T. Nakagawa and T. Kawai, Recent progress of luminescent metal complexes with photochromic units, *Coord. Chem. Rev.*, 2010, **254**, 2643–2651.

33 H. Nie, J. L. Self, A. S. Kuenstler, R. C. Hayward and J. Read de Alaniz, Multiaddressable Photochromic Architectures: From Molecules to Materials, *Adv. Opt. Mater.*, 2019, **7**, 1900224.

34 L. Norel, O. Galangau, H. Al Sabea and S. Rigaut, Remote Control of Near Infrared Emission with Lanthanide Complexes, *ChemPhotoChem*, 2021, **5**, 393–405.

35 R. Li, F.-F. Xu, Z.-L. Gong and Y.-W. Zhong, Thermo-responsive light-emitting metal complexes and related materials, *Inorg. Chem. Front.*, 2020, **7**, 3258–3281.

36 Y. Hasegawa and Y. Kitagawa, Thermo-sensitive luminescence of lanthanide complexes, clusters, coordination polymers and metal–organic frameworks with organic photosensitizers, *J. Mater. Chem. C*, 2019, **7**, 7494–7511.

37 M. Liberka, M. Zychowicz, L. Vasseur, J. Hooper and S. Chorazy, Governing efficiency and thermoresponsivity of luminescence in dirhenium(v) molecules by a highly tunable emission mechanism, *Inorg. Chem. Front.*, 2024, **11**, 8047–8069.

38 L. Labella, G. Bottaro, F. Marchetti, S. Samaritani and L. Armelao, Luminescent Tetrahedral Manganese(ii) Pentaphluorophenolate Complex as a Highly Sensitive Molecular Thermometer, *Inorg. Chem.*, 2025, **64**, 7960–7969.

39 D. Errulat, R. Marin, D. A. Gálico, K. L. M. Harriman, A. Pialat, B. Gabidullin, F. Iikawa, O. D. D. Couto Jr., J. O. Moilanen, E. Hemmer, F. A. Sigoli and M. Murugesu, A Luminescent Thermometer Exhibiting Slow Relaxation of the Magnetization: Toward Self-Monitored Building Blocks for Next-Generation Optomagnetic Devices, *ACS Cent. Sci.*, 2019, **5**, 1187–1198.

40 A. G. Bispo-Jr, D. A. Gálico, R. M. Diaz-Rodriguez, J. S. Ovens, F. A. Sigoli and M. Murugesu, The role of terminal ligands in the slow relaxation of magnetisation and luminescence thermometry of dinuclear NdIII complexes, *Inorg. Chem. Front.*, 2023, **10**, 3929–3939.

41 S. Zanella, M. Aragon-Alberti, C. D. S. Brite, F. Salles, L. D. Carlos and J. Long, Luminescent Single-Molecule Magnets as Dual Magneto-Optical Molecular Thermometers, *Angew. Chem., Int. Ed.*, 2023, **62**, e202306970.

42 J. Corredoira-Vázquez, C. González-Barreira, M. Fondo, A. M. García-Deibe, J. Sanmartín-Matalobos, S. Gómez-Coca, E. Ruiz, C. D. S. Brites and L. D. Carlos, An air-stable high-performance single-molecule magnet operating as a luminescent thermometer below its blocking temperature, *Inorg. Chem. Front.*, 2025, **12**, 5506–5516.

43 D. Marcinkowski, D. Prętka, P. Woźny, J. Kobylarczyk, A. Siwiak, D. Pakulski, V. Patroniak, K. Roszak, A. Katrusiak, R. Herchel, R. Podgajny, S. Sobczak, N. Majewska, S. Mahlik, M. Runowski and A. Gorczyński, Nd(iii)-Based Temperature-Independent Manometer and Pressure-Independent Thermometer with Slow Relaxation of Magnetization, *Adv. Opt. Mater.*, 2025, 2500495.

44 L.-R. Lin, X. Wang, G.-N. Wei, H.-H. Tang, H. Zhang and L.-H. Ma, Azobenzene-derived tris-β-diketonate lanthanide complexes: reversible trans-to-cis photoisomerization in solution and solid state, *Dalton Trans.*, 2016, **45**, 14954–14964.

45 L.-R. Lin, H.-H. Tang, Y.-G. Wang, X. Wang, X.-M. Fang and L.-H. Ma, Functionalized Lanthanide(iii) Complexes Constructed from Azobenzene Derivative and β-Diketone Ligands: Luminescent, Magnetic, and Reversible Trans-to-Cis Photoisomerization Properties, *Inorg. Chem.*, 2017, **56**, 3889–3900.

46 Y.-G. Wang, Y.-Q. Li, H.-H. Tang, L.-R. Lin and L.-H. Ma, Near-Infrared Photoluminescence and Reversible Trans-to-Cis Photoisomerization of Mononuclear and Binuclear Ytterbium(iii) Complexes Functionalized by Azobenzene Groups, *ACS Omega*, 2018, **3**, 5480–5490.

47 G. Huang, X. Yi, F. Gendron, B. Le Guennic, T. Guizouarn, C. Daiguebonne, G. Calvez, Y. Suffren, O. Guillou and K. Bernot, A supramolecular chain of dimeric Dy single molecule magnets decorated with azobenzene ligands, *Dalton Trans.*, 2019, **48**, 16053–16061.

48 C.-Y. Fu, L. Chen, X. Wang and L.-R. Lin, Synthesis of Bis-β-Diketonate Lanthanide Complexes with an Azobenzene Bridge and Studies of Their Reversible Photo/Thermal Isomerization Properties, *ACS Omega*, 2019, **4**, 15530–15538.

49 M. Cieslikiewicz-Bouet, S. V. Eliseeva, V. Aucagne, A. F. Delmas, I. Gillaizeau and S. Petoud, Near-infrared emitting lanthanide(iii) complexes as prototypes of optical imaging agents with peptide targeting ability: a methodological approach, *RSC Adv.*, 2019, **9**, 1747–1751.

50 J. Xie, T. Wu, X. Wang, C. Yu, W. Huang and D. Wu, Azo-Label Heterometal–Organic Rhomboids Exhibiting Photoswitchable NIR Luminescence in Crystalline State, *Inorg. Chem.*, 2020, **59**, 15460–15466.

51 C. Qian, Y. Ma, Y. Zhang, L. Yuan, D. Zhang, L. Zhao, J. Luo and X. Wang, A multi-input/multi-output molecular system based on lanthanide(iii) complexes, *Inorg. Chem. Front.*, 2022, **9**, 2668–2675.

52 A. Guesdon-Vennerie, P. Couvreur, F. Ali, F. Pouzoulet, C. Roulin, I. Martínez-Rovira, G. Bernadat, F.-X. Legrand, C. Bourgaux, C. L. Mazars, S. Marco, S. Trépout, S. Mura, S. Mériaux and G. Bort, Breaking photoswitch activation depth limit using ionising radiation stimuli adapted to clinical application, *Nat. Commun.*, 2022, **13**, 4102.

53 C. H. Simms, V. R. M. Nielsen, T. J. Sørensen, S. Faulkner and M. J. Langton, Photoswitchable luminescent lanthanide complexes controlled and interrogated by four orthogonal wavelengths of light, *Phys. Chem. Chem. Phys.*, 2024, **26**, 18683–18691.

54 A. J. Amoroso and S. J. A. Pope, Using lanthanide ions in molecular bioimaging, *Chem. Soc. Rev.*, 2015, **44**, 4723–4742.

55 K. Atal, U. Phageria, S. Kumari, Y. Dhayal and S. Bugalia, A review on designing and synthesis of lanthanide based macrocyclic complexes and their potential applications, *Inorg. Chim. Acta*, 2024, **561**, 121857.

56 W.-L. Zhou, Y. Chen, W. Lin and Y. Liu, Luminescent lanthanide–macrocycle supramolecular assembly, *Chem. Commun.*, 2021, **57**, 11443–11456.

57 Y. Gil, A. Castro-Alvarez, P. Fuentealba, E. Spodine and D. Aravena, Lanthanide SMMs Based on Belt Macrocycles: Recent Advances and General Trends, *Chem. – Eur. J.*, 2022, **28**, e202200336.

58 N. Su, J. S. Bradshaw, X. X. Zhang, P. B. Savage, K. E. Krakowiak and R. M. Izatt, Syntheses of diaza-18-crown-6 ligands containing two units each of 4-hydroxyazobenzene, benzimidazole, uracil, anthraquinone, or ferrocene groups, *J. Heterocycl. Chem.*, 1999, **36**, 771–775.

59 J. A. Peters, K. Djanashvili, C. F. G. C. Geraldes and C. Platas-Iglesias, The chemical consequences of the gradual decrease of the ionic radius along the Ln-series, *Coord. Chem. Rev.*, 2020, **406**, 213146.

60 S. Li, S. Jansone-Popova and D.-e. Jiang, Insights into coordination and ligand trends of lanthanide complexes from the Cambridge Structural Database, *Sci. Rep.*, 2024, **14**, 11301.

61 S. A. Cotton and P. R. Raithby, Systematics and surprises in lanthanide coordination chemistry, *Coord. Chem. Rev.*, 2017, **340**, 220–231.

62 A. Hu, S. N. MacMillan and J. J. Wilson, Macrocyclic Ligands with an Unprecedented Size-Selectivity Pattern for the Lanthanide Ions, *J. Am. Chem. Soc.*, 2020, **142**, 13500–13506.

63 A. Roca-Sabio, M. Mato-Iglesias, D. Esteban-Gómez, É. Tóth, A. d. Blas, C. Platas-Iglesias and T. Rodríguez-Blas, Macrocyclic Receptor Exhibiting Unprecedented Selectivity for Light Lanthanides, *J. Am. Chem. Soc.*, 2009, **131**, 3331–3341.

64 N. A. Thiele, V. Brown, J. M. Kelly, A. Amor-Coarasa, U. Jermilova, S. N. MacMillan, A. Nikolopoulou, S. Ponnala, C. F. Ramogida, A. K. H. Robertson, C. Rodríguez-Rodríguez, P. Schaffer, C. Williams Jr., J. W. Babich, V. Radchenko and J. J. Wilson, An Eighteen-Membered Macrocyclic Ligand for Actinium-225 Targeted Alpha Therapy, *Angew. Chem., Int. Ed.*, 2017, **56**, 14712–14717.

65 W.-C. Xu, S. Sun and S. Wu, Photoinduced Reversible Solid-to-Liquid Transitions for Photoswitchable Materials, *Angew. Chem., Int. Ed.*, 2019, **58**, 9712–9740.

66 P. Weis and S. Wu, Light-Switchable Azobenzene-Containing Macromolecules: From UV to Near Infrared, *Macromol. Rapid Commun.*, 2018, **39**, 1700220.

67 Y. Li, K.-H. Huang, N. M. Morato and R. G. Cooks, Glass surface as strong base, 'green' heterogeneous catalyst and degradation reagent, *Chem. Sci.*, 2021, **12**, 9816–9822.

68 Y. Li, T. F. Mehari, Z. Wei, Y. Liu and R. G. Cooks, Reaction Acceleration at Solid/Solution Interfaces: Katritzky Reaction Catalyzed by Glass Particles, *Angew. Chem., Int. Ed.*, 2021, **60**, 2929–2933.

69 H. M. D. Bandara and S. C. Burdette, Photoisomerization in different classes of azobenzene, *Chem. Soc. Rev.*, 2012, **41**, 1809–1825.

70 A. A. Beharry, O. Sadovski and G. A. Woolley, Azobenzene Photoswitching without Ultraviolet Light, *J. Am. Chem. Soc.*, 2011, **133**, 19684–19687.

71 M. Gao, D. Kwaria, Y. Norikane and Y. Yue, Visible-light-switchable azobenzenes: Molecular design, supramolecular systems, and applications, *Nat. Sci.*, 2023, **3**, e220020.

72 E. Nieland, J. Voss, A. Mix and B. M. Schmidt, Photoresponsive Dissipative Macrocycles Using Visible-Light-Switchable Azobenzenes, *Angew. Chem., Int. Ed.*, 2022, **61**, e202212745.

73 Y. Huang, X. Zeng, X. Ma, Z. Lin, J. Sun, W. Xiao, S. H. Liu, J. Yin and G.-F. Yang, A visible light-activated azo-fluorescent switch for imaging-guided and light-controlled release of antimycotics, *Nat. Commun.*, 2024, **15**, 8670.

74 J. Volarić, J. Buter, A. M. Schulte, K.-O. van den Berg, E. Santamaría-Aranda, W. Szymanski and B. L. Feringa, Design and Synthesis of Visible-Light-Responsive Azobenzene Building Blocks for Chemical Biology, *J. Org. Chem.*, 2022, **87**, 14319–14333.

75 K. Kuntze, J. Isokuortti, A. Siiskonen, N. Durandin, T. Laaksonen and A. Priimagi, Azobenzene Photoswitching with Near-Infrared Light Mediated by Molecular Oxygen, *J. Phys. Chem. B*, 2021, **125**, 12568–12573.

76 J. Baldwin, A. Brookfield, G. F. S. Whitehead, L. S. Natrajan, E. J. L. McInnes, M. S. Oakley and D. P. Mills, Isolation and Electronic Structures of Lanthanide(II) Bis(trimethylsilyl)phosphide Complexes, *Inorg. Chem.*, 2024, **63**, 18120–18136.

77 W. A. Rabanal-León, D. Páez-Hernández and R. Arratia-Pérez, Covalent lanthanide(iii) macrocyclic complexes: the bonding nature and optical properties of a promising single antenna molecule, *Phys. Chem. Chem. Phys.*, 2014, **16**, 25978–25988.

78 M. del C. Fernández-Fernández, R. Bastida, A. Macías, P. Pérez-Lourido, C. Platas-Iglesias and L. Valencia, Lanthanide(III) Complexes with a Tetrapyridine Pendant-Armed Macrocyclic Ligand: ^{1}H NMR Structural Determination in Solution, X-ray Diffraction, and Density-Functional Theory Calculations, *Inorg. Chem.*, 2006, **45**, 4484–4496.

79 A. Cruz-Navarro, J. M. Rivera, J. Durán-Hernández, S. Castillo-Blum, A. Flores-Parra, M. Sánchez, I. Hernández-Ahuactzi and R. Colorado-Peralta, Luminescence properties and DFT calculations of lanthanide(III) complexes (Ln = La, Nd, Sm, Eu, Gd, Tb, Dy) with 2,6-bis(5-methyl-benzimidazol-2-yl)pyridine, *J. Mol. Struct.*, 2018, 209–216.

80 J. Pang, C. Gao, L. Shu, X. Hu and M. Li, DFT calculations: Bridged-azo working with visible light, *Comput. Theor. Chem.*, 2020, **1191**, 113041.

81 Z. Wang, L. Heinke, J. Jelic, M. Cakici, M. Dommaschk, R. J. Maurer, H. Oberhofer, S. Grosjean, R. Herges, S. Bräse, K. Reuter and C. Wöll, Photoswitching in nanoporous, crystalline solids: an experimental and theoretical study for azobenzene linkers incorporated in MOFs, *Phys. Chem. Chem. Phys.*, 2015, **17**, 14582–14587.

82 C. D. S. Brites, R. Marin, M. Suta, A. N. Carneiro Neto, E. Ximendes, D. Jaque and L. D. Carlos, Spotlight on Luminescence Thermometry: Basics, Challenges, and Cutting-Edge Applications, *Adv. Mater.*, 2023, **35**, 2302749.

83 X. Qiu, T. Zheng, M. Runowski, P. Woźny, I. R. Martín, K. Soler-Carracedo, C. E. Piñero, S. Lebedkin, O. Fuhr and S. Bräse, Constructing [2.2]Paracyclophane-Based Ultrasensitive Optical Fluorescent-Phosphorescent Thermometer with Cucurbit[8]uril Supramolecular Assembly, *Adv. Funct. Mater.*, 2024, **34**, 2313517.

84 M. Runowski, A. Shyichuk, A. Tymiński, T. Grzyb, V. Lavín and S. Lis, Multifunctional Optical Sensors for Nanomanometry and Nanothermometry: High-Pressure and High-Temperature Upconversion Luminescence of Lanthanide-Doped Phosphates—LaPO4/YPO4:Yb3+–Tm3+, *ACS Appl. Mater. Int*, 2018, **10**, 17269–17279.

85 (*a*) D. Prętka, D. Marcinkowski, N. Vadra, P. Woźny, M. Runowski, M. Kubicki, V. Patroniak, G. Consiglio, G. Forte and A. Gorczyński, CCDC 2406250: Experimental Crystal Structure Determination, 2025, DOI: **10.5517/ccdc.csd.cc2lrwz7**; (*b*) D. Prętka, D. Marcinkowski, N. Vadra, P. Woźny, M. Runowski, M. Kubicki, V. Patroniak, G. Consiglio, G. Forte and A. Gorczyński, CCDC 2406251: Experimental Crystal Structure Determination, 2025, DOI: **10.5517/ccdc.csd.cc2lrx09**; (*c*) D. Prętka, D. Marcinkowski, N. Vadra, P. Woźny, M. Runowski, M. Kubicki, V. Patroniak, G. Consiglio, G. Forte and A. Gorczyński, CCDC 2406252: Experimental Crystal Structure Determination, 2025, DOI: **10.5517/ccdc.csd.cc2lrx1b**; (*d*) D. Prętka, D. Marcinkowski, N. Vadra, P. Woźny, M. Runowski, M. Kubicki, V. Patroniak, G. Consiglio, G. Forte and A. Gorczyński, CCDC 2406253: Experimental Crystal Structure Determination, 2025, DOI: **10.5517/ccdc.csd.cc2lrx2c**; (*e*) D. Prętka, D. Marcinkowski, N. Vadra, P. Woźny, M. Runowski, M. Kubicki, V. Patroniak, G. Consiglio, G. Forte and A. Gorczyński, CCDC 2406254: Experimental Crystal Structure Determination, 2025, DOI: **10.5517/ccdc.csd.cc2lrx3d**; (*f*) D. Prętka, D. Marcinkowski, N. Vadra, P. Woźny, M. Runowski, M. Kubicki, V. Patroniak, G. Consiglio, G. Forte and A. Gorczyński, CCDC 2406255: Experimental Crystal Structure Determination, 2025, DOI: **10.5517/ccdc.csd.cc2lrx4f**; (*g*) D. Prętka, D. Marcinkowski, N. Vadra, P. Woźny, M. Runowski, M. Kubicki, V. Patroniak, G. Consiglio, G. Forte and A. Gorczyński, CCDC 2406256: Experimental Crystal Structure Determination, 2025, DOI: **10.5517/ccdc.csd.cc2lrx5g**; (*h*) D. Prętka, D. Marcinkowski, N. Vadra, P. Woźny, M. Runowski, M. Kubicki, V. Patroniak, G. Consiglio, G. Forte and A. Gorczyński, CCDC 2406257: Experimental Crystal Structure Determination, 2025, DOI: **10.5517/ccdc.csd.cc2lrx6h**; (*i*) D. Prętka, D. Marcinkowski, N. Vadra, P. Woźny, M. Runowski, M. Kubicki, V. Patroniak, G. Consiglio, G. Forte and A. Gorczyński, CCDC 2406258: Experimental Crystal Structure Determination, 2025, DOI: **10.5517/ccdc.csd.cc2lrx7j**; (*j*) D. Prętka, D. Marcinkowski, N. Vadra, P. Woźny, M. Runowski, M. Kubicki, V. Patroniak, G. Consiglio, G. Forte and A. Gorczyński, CCDC 2435298: Experimental Crystal Structure Determination, 2025, DOI: **10.5517/ccdc.csd.cc2mr40k**; (*k*) D. Prętka, D. Marcinkowski, N. Vadra, P. Woźny, M. Runowski, M. Kubicki, V. Patroniak, G. Consiglio, G. Forte and A. Gorczyński, CCDC 2435299: Experimental Crystal Structure Determination, 2025, DOI: **10.5517/ccdc.csd.cc2mr41l**; (*l*) D. Prętka, D. Marcinkowski, N. Vadra, P. Woźny, M. Runowski, M. Kubicki, V. Patroniak, G. Consiglio, G. Forte and A. Gorczyński, CCDC 2480151: Experimental Crystal Structure Determination, 2025, DOI: **10.5517/ccdc.csd.cc2p7swm**.